MDPI

Numerical Modeling of Distortion of Ti-6Al-4V Components Manufactured Using Laser Powder Bed Fusion

Patiparn Ninpetch [1], Pruet Kowitwarangkul [1,*], Prasert Chalermkarnnon [2], Patcharapit Promoppatum [3], Piyapat Chuchuay [1] and Phadungsak Rattanadecho [4]

[1] The Sirindhorn International Thai-German Graduate School of Engineering (TGGS), King Mongkut's University of Technology North Bangkok (KMUTNB), Bangkok 10800, Thailand

[2] Assistive Technology and Medical Devices Research Center, National Science and Technology Development Agency (NSTDA), Pathum Thani 12120, Thailand

[3] Center for Lightweight Materials, Design, and Manufacturing, Department of Mechanical Engineering, Faculty of Engineering, King Mongkut's University of Technology Thonburi (KMUTT), Bangkok 10140, Thailand

[4] Department of Mechanical Engineering, Faculty of Engineering, Thammasat University (Rangsit Campus), Pathum Thani 12121, Thailand

[*] Correspondence: pruet.k@tggs.kmutnb.ac.th

Abstract: The laser powder bed fusion (L-PBF) process is a powder-based additive manufacturing process that can manufacture complex metallic components. However, when the metallic components are fabricated with the L-PBF process, they frequently encounter the residual stress and distortion that occurs due to the cyclic of rapid heating and cooling. The distortion detrimentally impacts the dimensional and geometrical accuracy of final built parts in the L-PBF process. The purpose of this research was to explore and predict the distortion of Ti-6Al-4V components manufactured using the L-PBF process by using numerical modeling in Simufact Additive 2020 FP1 software. Firstly, the numerical model validation was conducted with the twin-cantilever beam part. Later, studies were carried out to examine the effect of component sizes and support-structure designs on the distortion of tibial component produced by the L-PBF process. The results of this research revealed a good agreement between the numerical model and experiment data. In addition, the platform was extended to predict the distortion in the tibial component. Large distortion arose near the interface between the tibial tray and support structure due to the different stiffness between the solid bulk and support structure. The distortion of the tibial component increased with increasing component size according to the surface area of the tibial tray, and with increasing thickness of the tibial tray. Furthermore, the support-structure design plays an important role in distortion reduction in the L-PBF process. For example, the maximum distortion of the tibial component was minimized up to 44% when a block support-structure design with a height of 2.5 mm was used instead of the lattice-based support. The present study provides useful information to help the medical sector to manufacture effective medical components and reduce the chance of part failure from cracking in the L-PBF process.

Keywords: additive manufacturing; laser powder bed fusion; tibial component; titanium alloy; numerical modeling; distortion

1. Introduction

Ti-6Al-4V is a type of titanium alloy that has been extensively used to manufacture medical components due to its low density, high strength-to-weight ratio, excellent corrosion resistance, good mechanical strength, and good biocompatibility [1,2]. Examples of medical components made with Ti-6Al-4V include bone scaffolds, hip prostheses, tibial components, and joint replacements [3]. The components have complex shapes with porous

structures, and are generally implanted into the human body to replace a damaged biological structure. However, components with porous structure are mostly impossible to be produced by traditional processes. Hence, a laser powder bed fusion (L-PBF) process, which is a powder-based additive manufacturing method, is an emerging technology for manufacturing complex-geometry components [4–6]. This process can create three-dimensional components with full density by using a laser energy source to selectively melt the metal powder in a layer-by-layer addition [7–9]. However, when the metallic components are produced by L-PBF, they associate with complex thermal process due to the rapid heating and cooling cycles that result in large thermal gradients [10,11]. The occurrence of large thermal gradients during the L-PBF process gives rise to large thermal strain, leading to large thermal stress-induced distortion [10]. Moreover, the distortion in L-PBF is caused by the nonuniform expansion and contraction of melted and solidified layers during the building process [12]. The distortion, which is inevitable during the L-PBF process, is a major issue and a challenge to effectively producing the metal components with high geometric accuracy [8]. Nevertheless, the distortion can be alleviated by the determination of proper processing parameters, such as laser power (P), scanning speed (v), layer thickness (Lt), and scanning strategies [13,14]. Furthermore, the post-heat-treatment process, especially stress relief, is commonly used for stress relaxation and distortion mitigation upon the substrate removal [15,16].

In the last decade, the influence of processing parameters on distortion in the L-PBF process has been investigated by numerous researchers through experimental study and numerical modeling [17–21]. To numerically study the formation of residual stress and distortion in the L-PBF process, numerical models based on the finite-element method (FEM), including the thermomechanical model and the inherent strain method (ISM), are effective approaches. The thermomechanical model, which couples thermal and mechanical analysis, is usually applied to simulate the temperature histories that induced residual stress and distortion. Unfortunately, while this model can reveal complex relationships between process parameters and distortion, it is not suitable for macro- or part-level estimation. This is mainly due to drastic difference in spatial and temporal scales of the problem, leading to exceedingly high computational power requirements [22–24]. On the contrary, the inherent strain method (ISM) is a solely mechanical analysis, in which no thermal effects are calculated. It can be implemented to study and predict the residual stress and distortion in the macroscale and investigate the printing strategy optimization for minimizing residual stress and distortion in the L-PBF process [25]. Li et al. [26] developed a multiscale numerical modeling to predict part distortion of a twin-cantilever beam and found that the large tensile stress can appear on the top layers of the part with support on the solid substrate. Promoppatum and Yao [27] utilized numerical and experimental study to fully examine the influence of energy input and scanning length on residual stress reduction. The findings indicated that the residual stress was mainly dependent on the thermal histories and the surface temperature. Residual stress reduction can take place with higher surface temperatures generated from either high-energy input or small scanning length. Taufek et al. [28] analyzed the distortion of SS 316L SLM products using numerical modeling based on the inherent strain method (ISM). They concluded that a part built in a vertical direction can provide smaller residual stress than that of a part built in a horizontal direction. Xiaohui et al. [29] established the finite-element model to examine the influence of supporting structure design on residual stress in the overhanging structure of components in the SLM process of AlSi10Mg alloy. The results showed that when the contour-cone supporting structure was applied, the residual stresses in both X and Y directions were higher than those in contour-block and contour-entity supporting structures.

Most previous studies on part-scale modeling that assessed the residual stress and distortion in the L-PBF process focused on simple shapes, such as thin-walled structures, cubic samples, canonical samples, and cantilever beams, among others [30]. Table 1 presents the previous studies of part-scale modeling in the L-PBF process. It can be found that the part-scale modeling of distortion in complex shape parts produced by the L-PBF process

have scarcely been developed and examined. Furthermore, studies that have reported the size effects on distortion of component produced by the L-PBF process are limited. Hence, it is necessary to examine the size effects on distortion of components fabricated using the L-PBF process to obtain final parts with high geometric accuracy.

Table 1. Previous studies of part-scale model in SLM process. Reprinted with permission from refs. [10,15,22–24,27,31–45]. Copyright 2022 Elsevier.

No.	Part Geometry	Studies
1	Cantilever beam	[15,22,23,31–36] *
2	Cubic sample	[27,37,38]
3	Thin-walled part	[10,39,40]
4	Canonical sample	[24,32,41]
5	Complex shape parts	[42–45]

Noted: * Part geometry and support structure included.

Additionally, if there are overhanging surfaces in the components fabricated by L-PBF process, the support structure is generally required to support the overhanging surfaces and prevent part failure [29,46]. The support-structure design in the L-PBF process commonly involves numerous design parameters e.g., support types, support height, support radius, and support hatch distance. However, when the support structure is added during building process, the distortion will be significantly affected. Nevertheless, when an optimum support structure is selected, it may reduce or prevent the distortion of build components. Nonetheless, research on the effect of support-structure design parameters on distortion of build component in the L-PBF process is rare. Therefore, the effect of support-structure design on distortion was explored in the present research.

In this research, a macroscale modeling approach for the L-PBF process was proposed and implemented to investigate and predict the distortion of Ti-6Al-4V part manufactured by the L-PBF process. Firstly, the verification of the numerical model and mesh convergence analysis in this study were carried out with twin-cantilever beam parts. The details are explained in Section 3. Later, the effect of part sizes on the distortion of tibial component manufactured using the L-PBF process was investigated. In addition, the effect of support design on the distortion of tibial components was studied to mitigate the distortion. The numerical modeling was performed using the commercial software Simufact Additive 2020 FP1 (Simufact Engineering GmbH, Hamburg, Germany), based on the inherent strain method (ISM). The present numerical result was validated with the experiments reported by Siewert et al. [47]. The tibial component, an implant for the knee joint replacement, was selected as the build component in this study. The findings from this study are expected to serve as the guideline for medical sector to fabricate effective medical components with low geometric deviations.

2. Numerical Modeling

2.1. Mechanical Modeling

In mechanical analysis of the L-PBF process, the thermal histories obtained from the thermal analysis are subsequently applied to calculate the residual stress and distortion. A constitutive model for elastic (Hook's law) and plastic behavior is defined in the built material. Nevertheless, the thermal and phase transformation effects are neglected for the mechanical analysis based on ISM. A constitutive model as shown in Equation (1) is applied for mechanical analysis in the L-PBF process. The value of inherent strain $\{\varepsilon^*\}$ is defined as seen in Equation (2). Moreover, total strain including elastic, plastic, thermal, and phase transformation strains is described in Equation (3) [28]:

$$\sigma = [D]\left\{\varepsilon^{elastic}\right\} \tag{1}$$

where σ is Cauchy stress [MPa], D is the fourth order stiffness tensor, and $\varepsilon^{elastic}$ is elastic strain.

$$\{\varepsilon^*\} = \left\{\varepsilon^{total}\right\} - \left\{\varepsilon^{elastic}\right\} \tag{2}$$

$$\left\{\varepsilon^{total}\right\} = \left\{\varepsilon^{elastic}\right\} + \left\{\varepsilon^{plastic}\right\} + \left\{\varepsilon^{thermal}\right\} + \left\{\varepsilon^{phase}\right\} \tag{3}$$

where ε^{total} is total strain $\varepsilon^{plastic}$ is plastic strain, $\varepsilon^{thermal}$ is thermal strain, and ε^{phase} is phase transformation strain.

For the analysis of plastic strain in the Simufact additive software, the von Mises yield criteria and Prandtl–Reuss flow rule are used as shown in Equations (4) and (5) [25]:

$$f = \sigma_{VM} - \sigma_y \tag{4}$$

$$d\varepsilon^{plastic} = d\lambda \frac{\partial f}{\partial \sigma} \tag{5}$$

where f is yield function, σ_{VM} is von Mises stress [MPa], σ_y is yield stress [MPa], and $d\lambda$ is plastic multiplier.

2.2. Numerical Modeling for Distortion Analysis

To carry out the macroscale numerical modeling for distortion analysis of the tibial component in Simufact Additive software (2020 FP1 version, Simufact Engineering GmbH, Hamburg, Germany), five steps are mainly involved. As shown in Figure 1, the sequence is as follows: (1) importing a model, (2) generating support structure, (3) creating voxel mesh, (4) calculating simulation, and (5) obtaining the simulation result of the as-built stage. After generating support structures, the material properties of Ti-6Al-4V as listed in Table 2 were defined. The inherent strain values, layer parameters, and rotation parameters were also determined. The voxel element was created to analyze the distortion of the component. After the calculation process was completed, the numerical result of the tibial component's distortion at the as-built stage can be obtained [42].
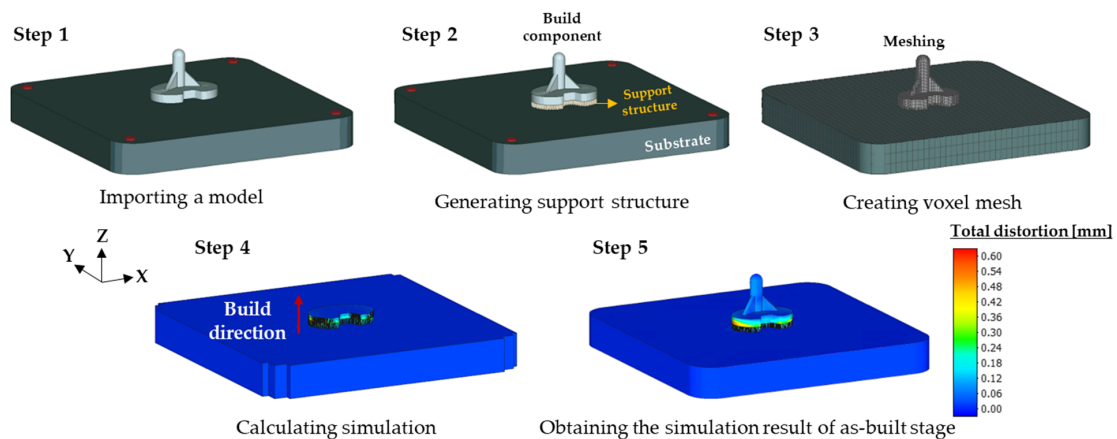

Figure 1. The sequence of numerical modeling using Simufact Additive in the present study.

Table 2. Dimensions of tibial components used in this study.

| Case Studies	Size **	Tray Thickness (T) (mm)	Length (L) (mm)	Width (W) (mm)	Height (H) (mm)	Tray Volume (mm³)	Code Name
1	S	8	60	40	43	14,516	S-T8
2	M	8	66	45	43	18,097	M-T8
3	L	8	72	50	43	22,034	L-T8
4	M	4	66	45	39	9049	M-T4
5	M	6	66	45	41	13,573	M-T6
6	M	10	66	45	45	22,622	M-T10

** S = small, M = medium, and L = large.

The Simufact Additive software, which is a scalable software solution for the metal additive manufacturing processes, requires the input of inherent strain values (ε^*) for calculation and prediction of the residual stress and part distortion. For the study, the inherent strains are acquired from the previous research of Siewert et al. [47]. Bidirectional scanning pattern is applied to build the twin-cantilever beam in the calibration process. The inherent strain values were calibrated by measuring cantilever distortion after cutting, and then the simulation model was calculated to match the experiment value. The inherent strain values in the X, Y, and Z directions are $\varepsilon_x^* = -0.0047$, $\varepsilon_y^* = -0.0020$, and $\varepsilon_z^* = 0$. The additional description of this calibration process can be found from [47]. Figure 2a shows the computational domain which consists of the build component, support structure, and substrate plate. Figure 2b shows the meshing of the computational domain.
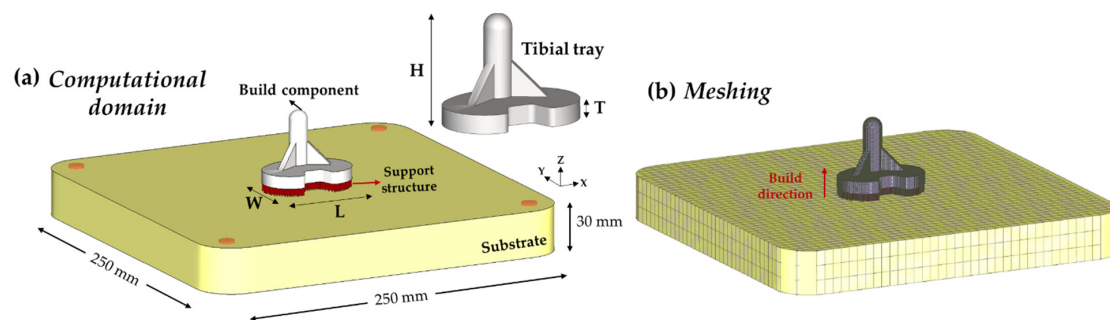

Figure 2. (**a**) Computational domain; (**b**) meshing.

The tibial components of all case studies were placed in the middle of the computational domain. The distance between the tibial component and substrate top surface of all cases was 5 mm. To explore the size effect on distortion in this study, rod support-structure design was used in all cases. The rod support radius was 0.3 mm, and the distance between each rod was 0.6 mm. The present study utilized voxel mesh number between 0.5 and 1.5 million elements. The initial temperature conditions were 298 K. The bottom of the substrate plate was set with zero displacement. As a result, the substrate is not allowed to move freely when the build components are produced. Figure 3 exhibits each size of the tibial component on the rod support. Table 2 presents the dimensions of the tibial components used in this study. The tibial component size S on the different support-structure designs is shown in Figure 4.
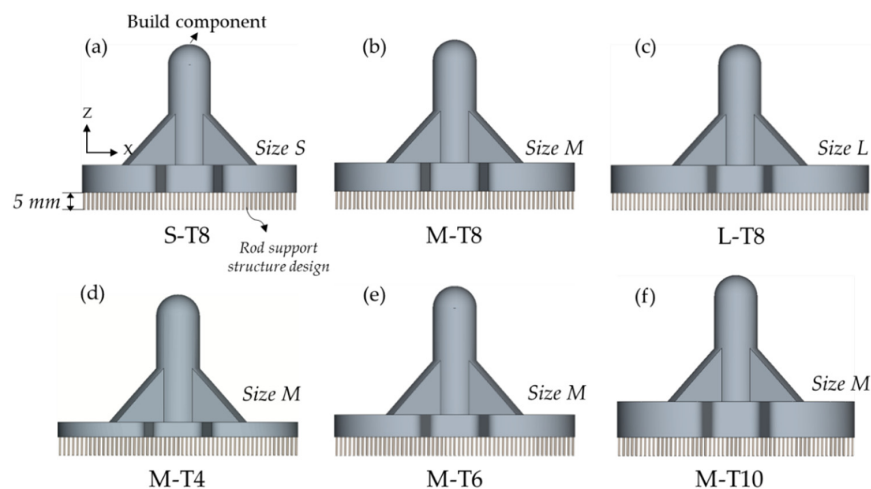

Figure 3. The model of each tibial component on the rod support structure with different tray sizes and tray thicknesses. (**a**) Small size with 8 mm thickness (S-T8); (**b**) Medium size with 8 mm thickness (M-T8); (**c**) Large size with 8 mm thickness (L-T8); (**d**) Medium size with 4 mm thickness (M-T4); (**e**) Medium size with 6 mm thickness (M-T6); (**f**) Medium size with 10 mm thickness (M-T10).
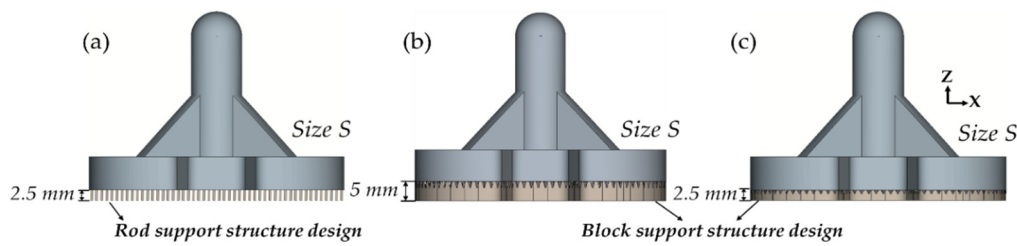
Figure 4. The model of tibial component with small size (S) on the different support -structure designs and support heights. (**a**) Rod support-structure design with height of 5 mm; (**b**) Block support-structure design with height of 5 mm; (**c**) Block support-structure design with height of 2.5 mm.

Figure 5 illustrates the patterns and dimensions of the support structure. The support volume for support-structure design with height of 5 mm case and height of 2.5 mm case were 1560 mm^3 and 780 mm^3 respectively.
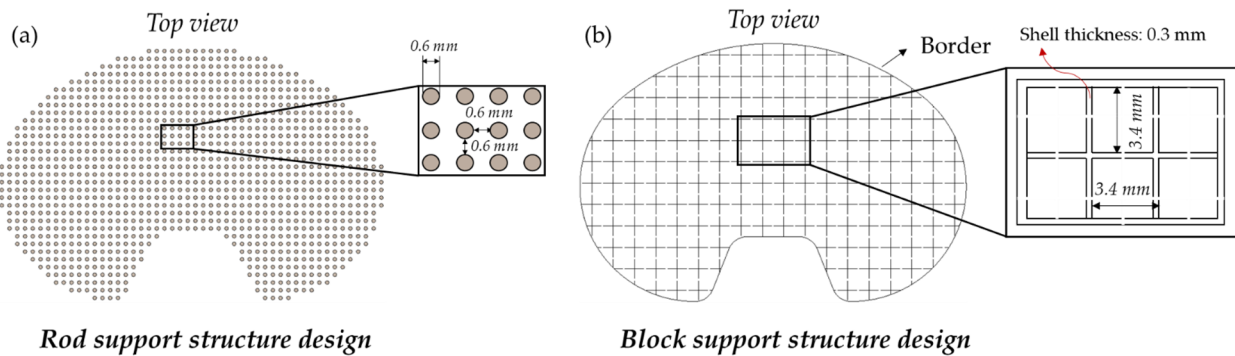
Figure 5. The pattern and dimensions of support structure: (**a**) Rod support-structure design; (**b**) Block support-structure design.

The material properties of Ti-6Al-4V alloys for the simulation were obtained from previous research of Siewert et al. [48] and the Simufact material database [49], as listed in Table 3. Table 4 tabulates the process parameters used for this study.

Table 3. Material properties of Ti-6Al-4V used for this study. Reprinted with permission from refs. [47,48]. Copyright 2022 Elsevier.

| Material Properties	Values
Density	4.4 g/cm^3
Young's modulus	110 GPa
Yield strength	1030 MPa
Poisson's ratio	0.31

Table 4. Process parameters used for this study. Reprinted with permission from ref. [47]. Copyright 2022 Elsevier.

Process Parameters	Values
Laser power	180 W
Scanning speed	1250 mm/s
Layer thickness	0.03 mm
Hatch spacing	0.105 mm

3. Model Validation

Mesh convergence analysis was initially performed to evaluate the influence of the number of elements on the simulation results and to obtain the reliability of the numer-

ical model. The twin-cantilever beam with dimensions of 7.5 mm (width) × 80 mm (length) × 13 mm (height) was used as a specimen, as illustrated in Figure 6a. The mesh convergence analysis was carried out by comparing the deflection measured at the middle point of the specimen, as illustrated in Figure 6b. The element sizes for the analysis were 0.6, 0.5, 0.4, 0.3, 0.25, and 0.2 mm. Each element size provided a total number of elements of 38,117, 56,691, 102,699, 224,901, 367,461, and 693,409, respectively. As illustrated in Figure 7, the simulation result can converge when the number of elements is greater than 100,000 elements. As a result, the element size of 0.25 mm was selected to further study the influence of part sizes and support-structure designs on the distortion of tibial component. In addition, to verify and obtain the accuracy of the numerical model implemented in this research, the result from numerical modeling in the present study was verified against the experiment from Siewert et al. [47]. Firstly, the twin-cantilever beam specimen as shown in Figure 6a has been printed with layer-by-layer addition. Then, the cantilever beam was removed from the substrate, where the deflection was seen due to the effect of stress relaxation. Figure 6b illustrates the comparison of the twin-cantilever beam distortion between the simulation result obtained from the present study and the experimental measurement from Siewert et al. [47]. It was found that the numerical result and the experiment result were in good agreement, with minor difference of 10.3%. Hence, the present numerical model can be used to investigate the distortion of the tibial component of the present study.
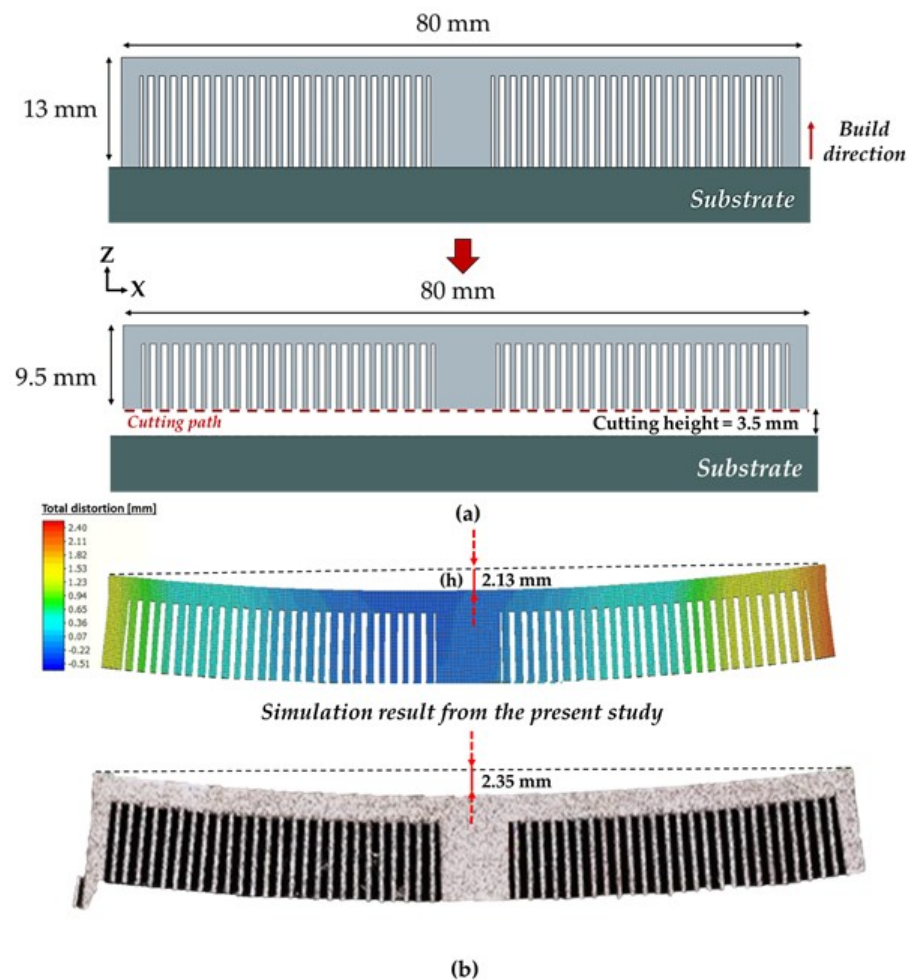
Figure 6. (**a**) The twin-cantilever beam with cutting path; (**b**) the comparison of the twin-cantilever beam distortion between simulation result obtained from the present study and the experimental study from Siewert et al. (experiment measurement modified from Siewert et al. [47]. Reproduced with license 5362460533296. Copyright 2022 Elsevier. (h) is the distance of the part's middle point on the surface to a line.
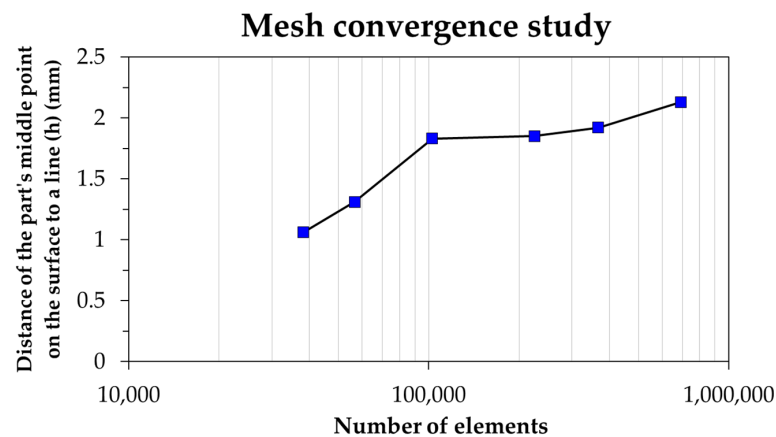
Figure 7. Mesh convergence study.

4. Results and Discussion

4.1. Distortion Distributions of Tibial Component

Figure 8 shows the total distortion distribution of the as-built S-T8 tibial component. The numerical results revealed that the large distortion occurred near the interface between the tibial tray and support structure. This is mainly due to the different stiffness of solid bulk and support structure. The maximum distortion arose around both edges of the long side of the tibial tray, which is marked in the red circles in Figure 8a. This region tended to be more susceptible to cracking. Meanwhile, the small distortion magnitude took place at the stem region and top surface of the tibial tray (blue region). In addition, it was noticed that the distortion magnitude gradually mitigated from the edge to the inside, as displayed in Figure 8c. Figure 8b amplifies the distortion at the edge region. It was observed that the distortion magnitude gradually decreased from the bottom surface at the interface to the top surface of the tibial tray because the constraint strength provided by the support structure decreased when the deposition height was increased. The black solid line in Figure 8b demonstrates the original shape of the tibial component.
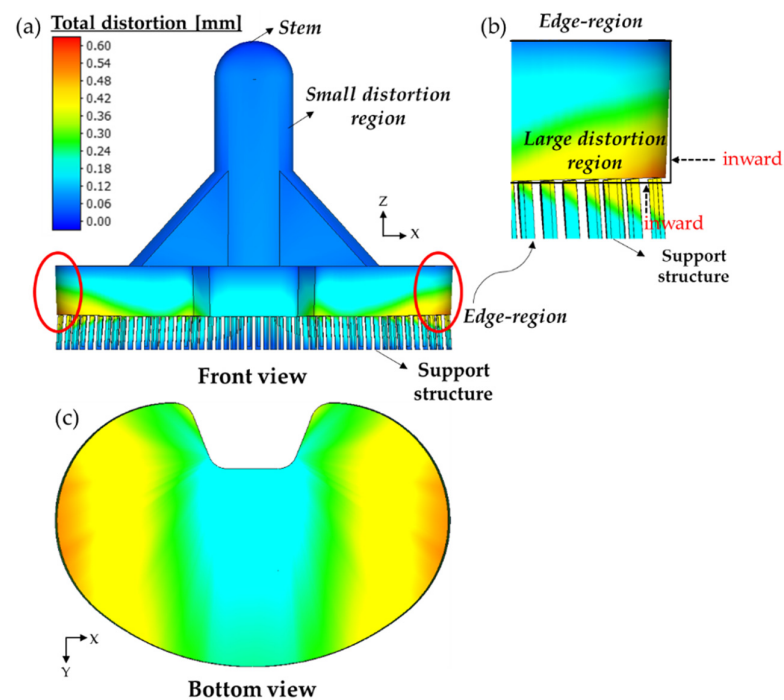

Figure 8. Total distortion distribution of the as-built S-T8 tibial component. (**a**) Front view; (**b**) Amplify the distortion at the edge region; (**c**) Bottom view.

Figure 9 exhibits the distortion distribution in each direction of the as-built S-T8 tibial component. The magnitude of distortion of the built component is represented by a color contour plot. The result revealed that the distortion distribution of the tibial component was different in each direction. According to the distortion distribution in the X-direction, the tibial component distorted inwardly at both edges of the tibial tray. The value of maximum distortion in the X-direction was around 0.34 mm, while the distortion value in the Y-direction was relatively less where its maximum magnitude was around 0.07 mm. It can be seen that the distortion magnitude in the Z-direction, which was along the build direction, was higher than that in the X- and Y-directions. The maximum distortion magnitude in the Z-direction was around 0.43 mm.
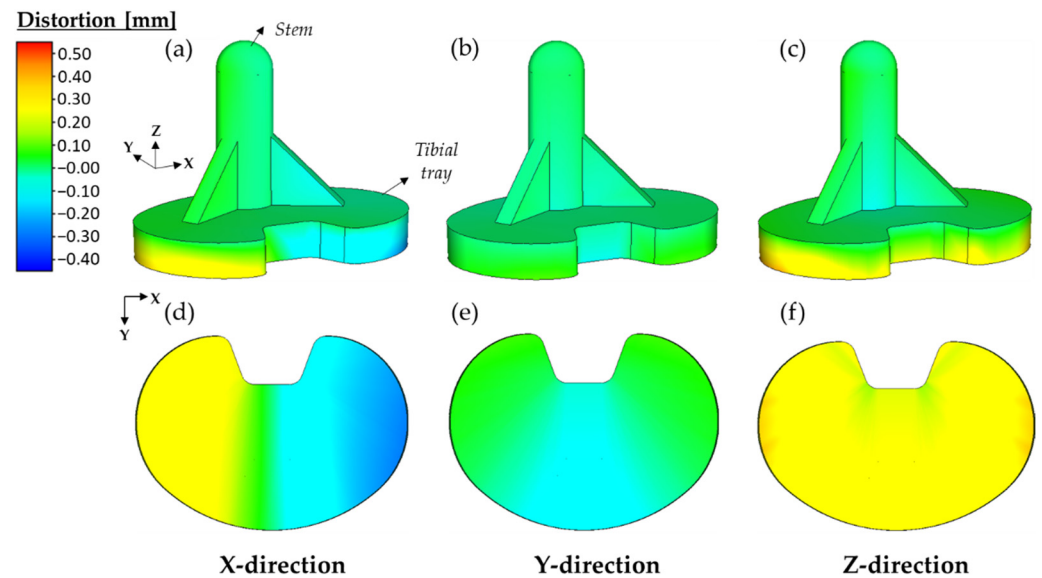
Figure 9. Distortion distribution in each direction of the as-built S-T8 tibial component. (**a**,**d**) X-direction; (**b**,**e**) Y-direction; (**c**,**f**) Z-direction.

4.2. Effect of Part Sizes on the Distortion of Tibial Component

Figure 10 shows the total distortion of the as-built tibial component with different sizes. The distortion distributions of all cases were similar, but the distortion in each case was different.
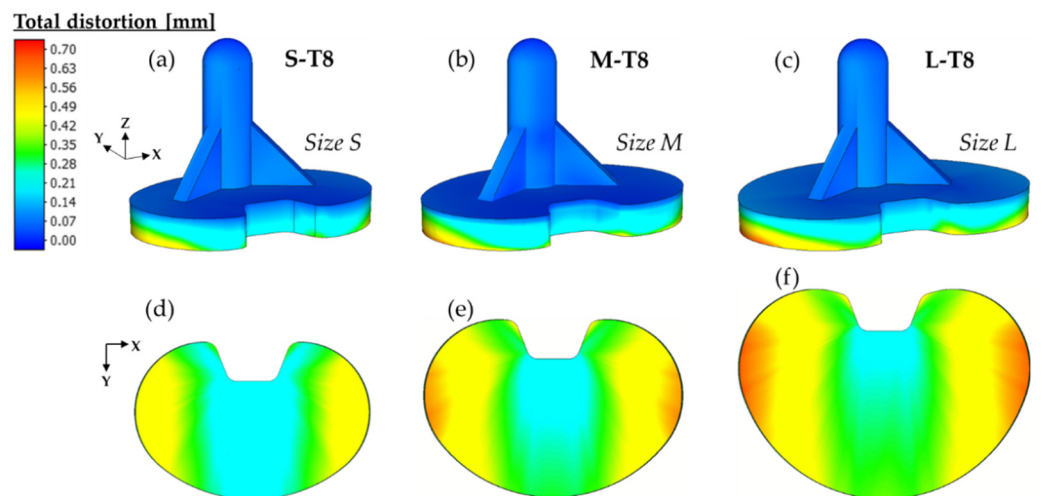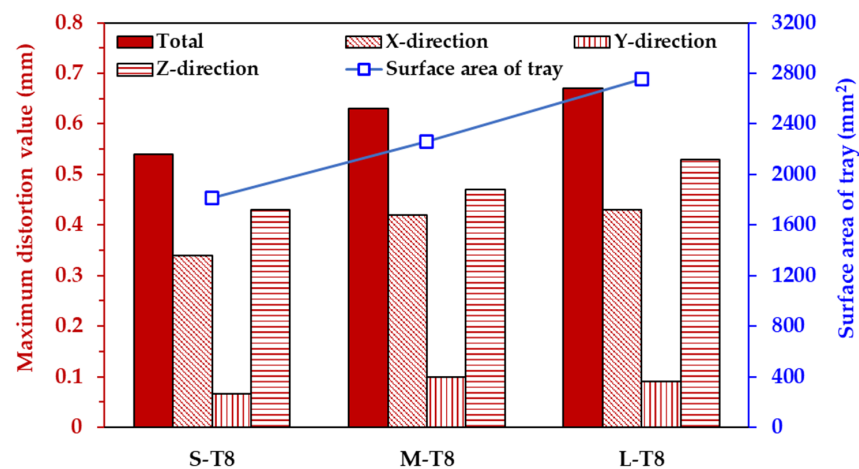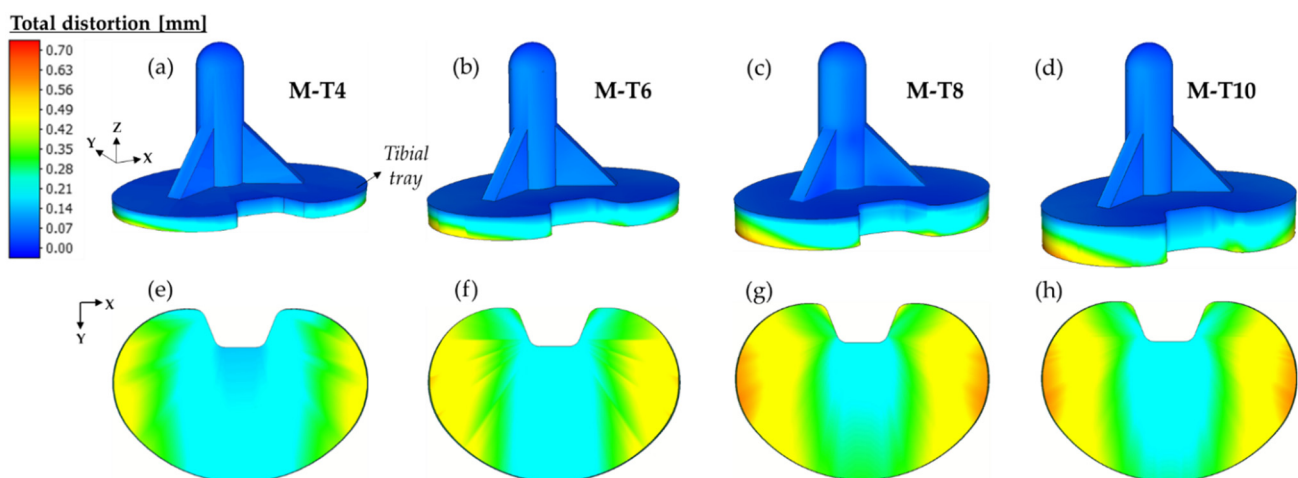
Figure 10. Total distortion of the as-built tibial component with different sizes. (**a**,**d**) Small size with 8 mm thickness (S-T8); (**b**,**e**) Medium size with 8 mm thickness (M-T8); (**c**,**f**) Large size with 8 mm thickness (M-T8).

The results indicated that the distortion of the tibial component tends to increase with larger size according to the surface area of the tibial tray. This is due to the shrinkage of the component that was approximately proportional to the part size and the influence of constraining strength between the built component and support structure [39,49]. As shown in Figure 11, the maximum total distortions of the tibial component of S-T8, M-T8, and L-T8 were 0.54 mm, 0.63 mm, and 0.67 mm, respectively. It can be noticed that when the component size was increased from small size (S) with the tibial tray surface area of 1815 mm^2 to medium size (M) with the tibial tray surface area of 2262 mm^2 and large size (L) with the tibial tray surface area of 2754 mm^2, the maximum total distortion was increased by 16.7% and 24.1% respectively. It was also discovered that the distortion in the Z-direction is more dominant than that in the X- and Y-directions. A similar result was also reported by Shi et al. [50].
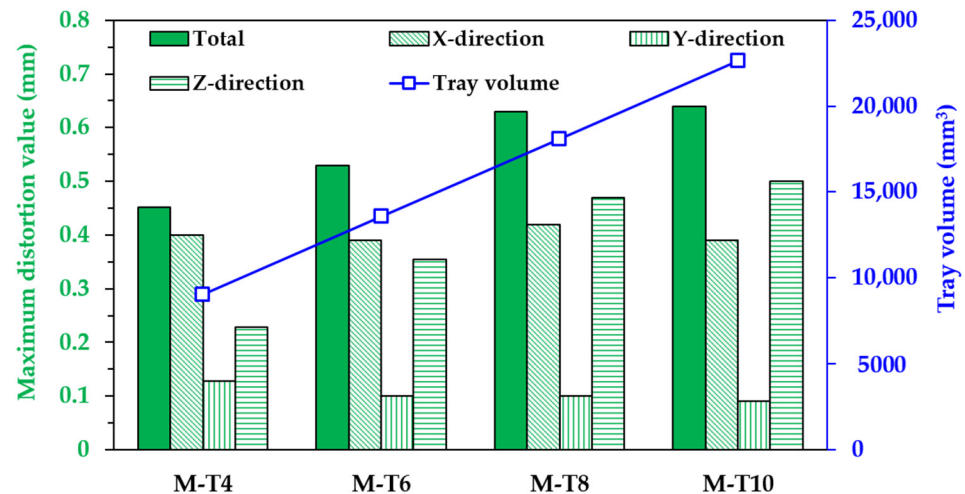

Figure 11. The maximum distortion of as-built tibial component fabricated by different sizes.

Figure 12 exhibits the total distortion at the as-built stage of medium-size tibial components with different tray thicknesses. The numerical result showed that the distortion distributions of all cases were similar. The distortion of the tibial component increases with the increasing thickness of the tibial tray, but has an insignificant effect on the higher thickness component.

Figure 12. The total distortion at the as-built stage of medium-size tibial component with different tray thickness. (**a,e**) Medium size with 4 mm thickness (M-T4); (**b,f**) Medium size with 6 mm thickness (M-T6); (**c,g**) Medium size with 8 mm thickness (M-T8); (**d,h**) Medium size with 10 mm thickness (M-T10).

Figure 13 illustrates the maximum distortion of the as-built tibial component with different tray thickness. The maximum total distortion value of the tibial component fabricated with different thicknesses of the tibial tray was 0.45 mm for M-T4, 0.53 mm for M-T6, 0.63 mm for M-T8, and 0.64 mm for M-T10. It was noted that when the thickness of the tray increased from 4 mm (M-T4) with tray volume of 9049 mm^3 to 6 mm (M-T6) with tray volume of 13,573 mm^3, 8 mm (M-T8) with tray volume of 18,097 mm^3 and 10 mm (M-T10) with tray volume of 22,622 mm^3, the maximum total distortion value of the tibial component was increased by 17.3%, 39.4%, and 41.6% respectively. This is because of the decrease in constraint strength with an increase in the thickness of the tibial tray.


Figure 13. The maximum distortion of the as-built tibial component with different tray thickness.

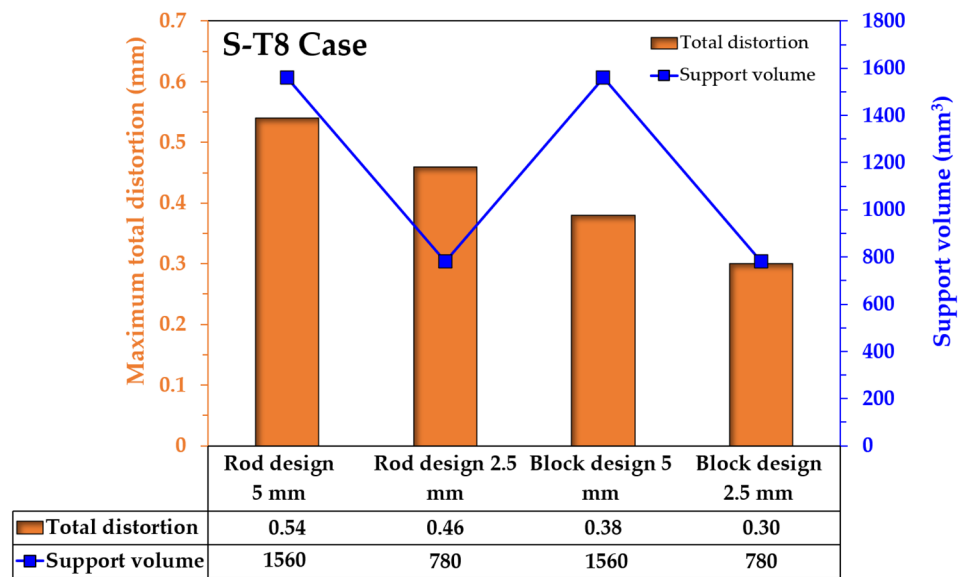### 4.3. Effect of Support-Structure Design on the Distortion of Tibial Component

A further study is the investigation of the effect of support-structure design on the distortion of the tibial component. It can be seen that the support-structure design plays an important role in the reduction of distortion in Figure 14. When the height of the support was decreased, the lower distortion of the tibial component and less material usage can be obtained. However, the difficulty of the build part and support removal should be noted. Meanwhile, usage of the proper design of the support structure, such as block structure instead of the lattice-based, or rod structure, provided a more effective distortion reduction than decreasing the support height, as illustrated in Figure 14c,d. The case with block support-structure design with the height of 2.5 mm has a minimum total distortion. This is due to the influence of support-structure stiffness.

Figure 15 illustrates the maximum total distortion value of the S-T8 tibial component fabricated under different support-structure designs. The result showed that the maximum distortion value of the S-T8 tibial component was reduced by 14.8% when the height of the rod support structure was lowered from 5 to 2.5 mm. While changing the support design from rod structure to block structure, the maximum distortion value of the S-T8 tibial component was reduced by 29.6% with the same height of 5mm, and 44.4% with the lower height of 2.5 mm.

Nonetheless, the support structure must be eliminated after the printing and cutting process. Generally, the support removal process can be done manually. The support structure in the L-PBF process was commonly eliminated from the solid substrate plate by the metal-cutting methods, such as wire EDM and milling [51]. Therefore, an optimum support-structure design that can be easily removed from the substrate plate should be carried out for reduction of the support removal time in subsequent work.
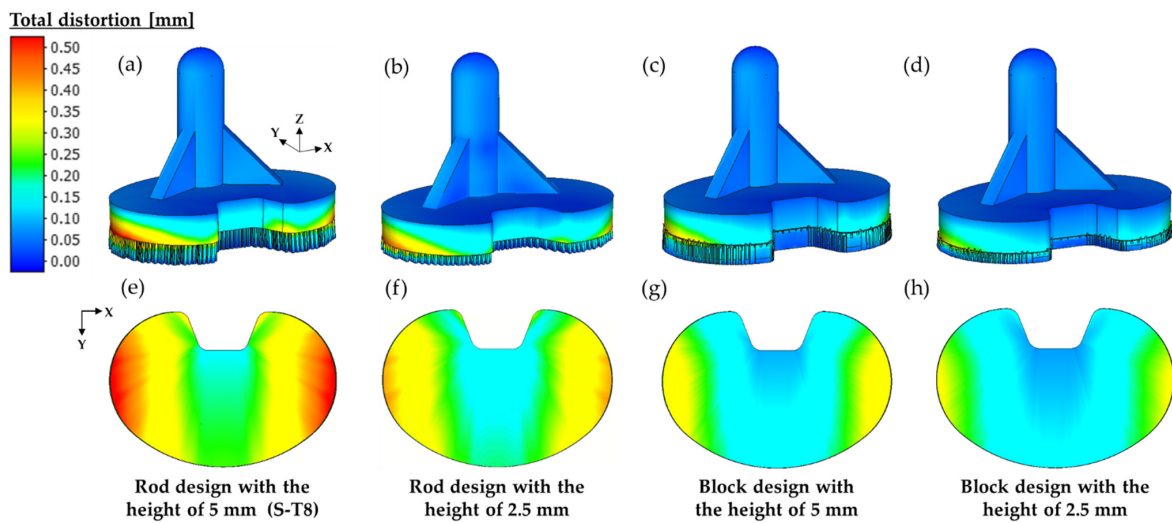
Figure 14. Total distortion distribution of as-built tibial component with different support structures and support heights. (**a**,**e**) Rod support-structure design with height of 5 mm (S-T8); (**b**,**f**) Rod support-structure design with height of 2.5 mm; (**c**,**g**) Block support-structure design with height of 5 mm; (**d**,**h**) Block support-structure design with the height of 2.5 mm.

	Rod design 5 mm	Rod design 2.5 mm	Block design 5 mm	Block design 2.5 mm
Total distortion	0.54	0.46	0.38	0.30
Support volume	1560	780	1560	780

Figure 15. The maximum total distortion of the S-T8 tibial component fabricated with different support structures.

5. Conclusions

The present study investigated the effect of part sizes and support-structure designs on the distortion of the tibial component fabricated by the L-PBF process using macroscale numerical modeling with the inherent strain method (ISM), in which the thermal effect was not considered. Numerical modeling was conducted with Simufact Additive 2020 FP1 software. The main results of the present study can be summarized as follows:

1. The large distortion takes place near the interface between the tibial tray and support structure because of the different stiffness between solid bulk and support structure. The maximum distortion occurs around both edges of the long side of the tibial tray. In addition, the distortion value in the Z-direction was greater than that of the X- and Y-directions.

2.　The distortion of the tibial component increases with the larger size according to the surface area of the tibial tray. The thickness of the tibial tray tends to increase the distortion of the component, but has less effect on the higher thickness component.

3.　The support-structure design plays a significant role in distortion reduction. Decreasing the height of the support gives lower distortion and less material usage, while the difficulty of the part removal should be considered. Applying an appropriate design of the support, such as block structure instead of rod structure, gives a more effective reduction of the distortion than decreasing the support height.

Institutional Review Board Statement: Not applicable.

Informed Consent Statement: Not applicable.

Data Availability Statement: Not applicable.

Conflicts of Interest: The authors declare no conflict of interest.

References

1.　Shipley, H.; McDonnell, D.; Culleton, M.; Coull, R.; Lupoi, R.; O'Donnell, G.; Trimble, D. Optimisation of Process Parameters to Address Fundamental Challenges during Selective Laser Melting of Ti-6Al-4V: A Review. *Int. J. Mach. Tools Manuf.* **2018**, *128*, 1–20. [CrossRef]

2.　Agius, D.; Kourousis, K.; Wallbrink, C. A Review of the As-Built SLM Ti-6Al-4V Mechanical Properties towards Achieving Fatigue Resistant Designs. *Metals* **2018**, *8*, 75. [CrossRef]

3.　Bai, L.; Gong, C.; Chen, X.; Sun, Y.; Zhang, J.; Cai, L.; Zhu, S.; Xie, S.Q. Additive Manufacturing of Customized Metallic Orthopedic Implants: Materials, Structures, and Surface Modifications. *Metals* **2019**, *9*, 1004. [CrossRef]

4.　Ninpetch, P.; Kowitwarangkul, P.; Mahathanabodee, S.; Chalermkarnnon, P.; Rattanadecho, P. Computational Investigation of Thermal Behavior and Molten Metal Flow with Moving Laser Heat Source for Selective Laser Melting Process. *Case Stud. Therm. Eng.* **2021**, *24*, 100860. [CrossRef]

5.　Bayat, M.; Mohanty, S.; Hattel, J.H. Multiphysics Modelling of Lack-of-Fusion Voids Formation and Evolution in IN718 Made by Multi-Track/Multi-Layer L-PBF. *Int. J. Heat Mass Transf.* **2019**, *139*, 95–114. [CrossRef]

6.　Ninpetch, P.; Kowitwarangkul, P. A Numerical Study on the Thermal Transient Model with Moving Laser Heat Source of AISI 304 Stainless Steel Plate. *Mater. Today Proc.* **2019**, *17*, 1761–1767. [CrossRef]

7.　Ninpetch, P.; Teenok, N.; Kowitwarangkul, P.; Mahathanabodee, S.; Tongsri, R.; Ratanadecho, P. The Influence of Laser Parameters on the Melted Track and Microstructure of AISI 316L Fabricated by L-PBF Process. In Proceedings of the 8th Asia Pacific IIW International Congress 2019, Bangkok, Thailand, 20–22 March 2019; pp. 39–43.

8.　Ninpetch, P.; Chalermkarnnon, P.; Kowitwarangkul, P. Multiphysics Simulation of Thermal-Fluid Behavior in Laser Powder Bed Fusion of H13 Steel: Influence of Layer Thickness and Energy Input. *Met. Mater. Int.* **2022**, 1–16. [CrossRef]

9.　Ninpetch, P.; Kowitwarangkul, P.; Mahathanabodee, S.; Chalermkarnnon, P.; Ratanadecho, P. A Review of Computer Simulations of Metal 3D Printing. *AIP Conf. Proc.* **2020**, *2279*, 050002. [CrossRef]

10.　Lu, X.; Chiumenti, M.; Cervera, M.; Tan, H.; Lin, X.; Wang, S. Warpage Analysis and Control of Thin-Walled Structures Manufactured by Laser Powder Bed Fusion. *Metals* **2021**, *11*, 686. [CrossRef]

11.　Botha, H.; Marais, D.; Kloppers, C.P. The Efficacy of The Inherent Strain Method in Determining Residual Stress in In718 SLM Specimens. *S. Afr. J. Ind. Eng.* **2021**, *32*, 264–278. [CrossRef]

12. Mugwagwa, L.; Dimitrov, D.; Matope, S.; Muvunzi, R. Residual Stresses and Distortions in Selective Laser Meltinga Review. In Proceedings of the 17th Rapid Product Development Association of South Africa, Vanderbijlpark, South Africa, 2–4 November 2016.

13. Ninpetch, P.; Kowitwarangkul, P.; Mahathanabodee, S.; Tongsri, R.; Ratanadecho, P. Thermal and Melting Track Simulations of Laser Powder Bed Fusion (L-PBF). *IOP Conf. Ser. Mater. Sci. Eng.* **2019**, *526*, 012030. [CrossRef]

14. DebRoy, T.; Wei, H.L.; Zuback, J.S.; Mukherjee, T.; Elmer, J.W.; Milewski, J.O.; Beese, A.M.; Wilson-Heid, A.; De, A.; Zhang, W. Additive Manufacturing of Metallic ComponentsProcess, Structure and Properties. *Prog. Mater. Sci.* **2018**, *92*, 112–224. [CrossRef]

15. De Baere, D.; Van Cauwenbergh, P.; Bayat, M.; Mohanty, S.; Thorborg, J.; Thijs, L.; Van Hooreweder, B.; Vanmeensel, K.; Hattel, J.H. Thermo-Mechanical Modelling of Stress Relief Heat Treatments after Laser-Based Powder Bed Fusion. *Addit. Manuf.* **2021**, *38*, 101818. [CrossRef]

16. Li, K.; Ma, R.; Zhang, M.; Chen, W.; Li, X.; Zhang, D.Z.; Tang, Q.; Murr, L.E.; Li, J.; Cao, H. Hybrid Post-Processing Effects of Magnetic Abrasive Finishing and Heat Treatment on Surface Integrity and Mechanical Properties of Additively Manufactured Inconel 718 Superalloys. *J. Mater. Sci. Technol.* **2022**, *128*, 10–21. [CrossRef]

17. Yakout, M.; Elbestawi, M.A.; Veldhuis, S.C.; Nangle-Smith, S. Influence of Thermal Properties on Residual Stresses in SLM of Aerospace Alloys. *Rapid Prototyp. J.* **2020**, *26*, 213–222. [CrossRef]

18. Ahmed, A.; Majeed, A.; Atta, Z.; Jia, G. Dimensional Quality and Distortion Analysis of Thin-Walled Alloy Parts of AlSi10Mg Manufactured by Selective Laser Melting. *J. Manuf. Mater. Process* **2019**, *3*, 51. [CrossRef]

19. Bian, P.; Shi, J.; Liu, Y.; Xie, Y. Influence of Laser Power and Scanning Strategy on Residual Stress Distribution in Additively Manufactured 316L Steel. *Opt. Laser Technol.* **2020**, *132*, 106477. [CrossRef]

20. Han, Q.; Gu, H.; Soe, S.; Setchi, R.; Lacan, F.; Hill, J. Manufacturability of AlSi10Mg Overhang Structures Fabricated by Laser Powder Bed Fusion. *Mater. Des.* **2018**, *160*, 1080–1095. [CrossRef]

21. Hajnys, J.; Pagáč, M.; Měsíček, J.; Petru, J.; Król, M. Influence of Scanning Strategy Parameters on Residual Stress in the SLM Process According to the Bridge Curvature Method for AISI 316L Stainless Steel. *Materials* **2020**, *13*, 1659. [CrossRef]

22. Setien, I.; Chiumenti, M.; van der Veen, S.; San Sebastian, M.; Garciandía, F.; Echeverría, A. Empirical Methodology to Determine Inherent Strains in Additive Manufacturing. *Comput. Math. Appl.* **2019**, *78*, 2282–2295. [CrossRef]

23. Bugatti, M.; Semeraro, Q. Limitations of the Inherent Strain Method in Simulating Powder Bed Fusion Processes. *Addit. Manuf.* **2018**, *23*, 329–346. [CrossRef]

24. Soylemez, E.; Koç, E.; Coşkun, M. Thermo-mechanical simulations of selective laser melting for AlSi10Mg alloy to predict the part-scale deformations. *Prog. Addit. Manuf.* **2019**, *4*, 465–478. [CrossRef]

25. Liang, X.; Cheng, L.; Chen, Q.; Yang, Q.; To, A.C. A Modified Method for Estimating Inherent Strains from Detailed Process Simulation for Fast Residual Distortion Prediction of Single-Walled Structures Fabricated by Directed Energy Deposition. *Addit. Manuf.* **2018**, *23*, 471–486. [CrossRef]

26. Li, C.; Liu, J.F.; Fang, X.Y.; Guo, Y.B. Efficient Predictive Model of Part Distortion and Residual Stress in Selective Laser Melting. *Addit. Manuf.* **2017**, *17*, 157–168. [CrossRef]

27. Promoppatum, P.; Yao, S.-C. Influence of Scanning Length and Energy Input on Residual Stress Reduction in Metal Additive Manufacturing: Numerical and Experimental Studies. *J. Manuf. Process.* **2020**, *49*, 247–259. [CrossRef]

28. Taufek, T.; Manurung, Y.H.; Lüder, S.; Graf, M.; Salleh, F.M. Distortion Analysis of SLM Product of SS316L Using Inherent Strain Method. *IOP Conf. Ser. Mater. Sci. Eng.* **2020**, *834*, 012011. [CrossRef]

29. Xiaohui, J.; Chunbo, Y.; Honglan, G.; Shan, G.; Yong, Z. Effect of Supporting Structure Design on Residual Stresses in Selective Laser Melting of AlSi10Mg. *Int. J. Adv. Manuf. Technol.* **2022**, *118*, 1597–1608. [CrossRef]

30. Bompos, D.; Chaves-Jacob, J.; Sprauel, J.-M. Shape Distortion Prediction in Complex 3D Parts Induced during the Selective Laser Melting Process. *CIRP Ann. Manuf. Technol.* **2020**, *69*, 517–520. [CrossRef]

31. Zhang, X.; Kang, J.; Rong, Y.; Wu, P.; Feng, T. Effect of Scanning Routes on the Stress and Deformation of Overhang Structures Fabricated by SLM. *Materials* **2018**, *12*, 47. [CrossRef]

32. Chen, Q.; Liang, X.; Hayduke, D.; Liu, J.; Cheng, L.; Oskin, J.; Whitmore, R.; To, A.C. An Inherent Strain Based Multiscale Modeling Framework for Simulating Part-Scale Residual Deformation for Direct Metal Laser Sintering. *Addit. Manuf.* **2019**, *28*, 406–418. [CrossRef]

33. Liang, X.; Hayduke, D.; To, A.C. An Enhanced Layer Lumping Method for Accelerating Simulation of Metal Components Produced by Laser Powder Bed Fusion. *Addit. Manuf.* **2021**, *39*, 101881. [CrossRef]

34. Xing, W.; Ouyang, D.; Li, N.; Liu, L. Estimation of Residual Stress in Selective Laser Melting of a Zr-Based Amorphous Alloy. *Materials* **2018**, *11*, 1480. [CrossRef] [PubMed]

35. Liang, X.; Chen, Q.; Cheng, L.; Hayduke, D.; To, A.C. Modified Inherent Strain Method for Efficient Prediction of Residual Deformation in Direct Metal Laser Sintered Components. *Comput. Mech.* **2019**, *64*, 1719–1733. [CrossRef]

36. De Baere, D.; Moshiri, M.; Smolej, L.; Hattel, J.H. Numerical Investigation into Laser-Based Powder Bed Fusion of Cantilevers Produced in 300-Grade Maraging Steel. *Addit. Manuf.* **2022**, *50*, 102560. [CrossRef]

37. Promoppatum, P.; Uthaisangsuk, V. Part Scale Estimation of Residual Stress Development in Laser Powder Bed Fusion Additive Manufacturing of Inconel 718. Finite Elem. *Anal. Des.* **2021**, *189*, 103528. [CrossRef]

38. Yakout, M.; Elbestawi, M.A.; Veldhuis, S.C. A Study of the Relationship between Thermal Expansion and Residual Stresses in Selective Laser Melting of Ti-6Al-4V. *J. Manuf. Process.* **2020**, *52*, 181–192. [CrossRef]

39. Chen, C.; Xiao, Z.; Zhu, H.; Zeng, X. Deformation and Control Method of Thin-Walled Part during Laser Powder Bed Fusion of Ti–6Al–4V Alloy. *Int. J. Adv. Manuf. Technol.* **2020**, *110*, 3467–3478. [CrossRef]
40. Yang, T.; Xie, D.; Yue, W.; Wang, S.; Rong, P.; Shen, L.; Zhao, J.; Wang, C. Distortion of Thin-Walled Structure Fabricated by Selective Laser Melting Based on Assumption of Constraining Force-Induced Distortion. *Metals* **2019**, *9*, 1281. [CrossRef]
41. Gouge, M.; Denlinger, E.; Irwin, J.; Li, C.; Michaleris, P. Experimental Validation of Thermo-Mechanical Part-Scale Modeling for Laser Powder Bed Fusion Processes. *Addit. Manuf.* **2019**, *29*, 100771. [CrossRef]
42. Pagac, M.; Hajnys, J.; Halama, R.; Aldabash, T.; Mesicek, J.; Jancar, L.; Jansa, J. Prediction of Model Distortion by FEM in 3D Printing via the Selective Laser Melting of Stainless Steel AISI 316L. *Appl. Sci.* **2021**, *11*, 1656. [CrossRef]
43. Gao, S.; Tan, Z.; Lan, L.; He, B. Effects of Geometrical Size and Structural Feature on the Shape-Distortion Behavior of Hollow Ti-Alloy Blade Fabricated by Additive Manufacturing Process. *J. Laser Appl.* **2020**, *32*, 032005. [CrossRef]
44. Gao, S.; Tan, Z.; Lan, L.; Lu, G.; He, B. Experimental Investigation and Numerical Simulation of Residual Stress and Distortion of Ti6Al4V Components Manufactured Using Selective Laser Melting. *J. Mater. Eng. Perform.* **2022**, 1–11. [CrossRef]
45. Jia, H.; Sun, H.; Wang, H.; Wu, Y.; Wang, H. Size Effect in Selective Laser Melting Additive Manufacturing of 700 mm Large Component. *J. Manuf. Process.* **2022**, *75*, 125–137. [CrossRef]
46. Sulaiman, M.R.; Yusof, F.; Jamaludin, M.F.B. Effect of Support Structure Design on the Part Built Using Selective Laser Melting. In *Advances in Material Sciences and Engineering*; Awang, M., Emamian, S.S., Yusof, F., Eds.; Springer: Singapore, 2020; pp. 275–286. ISBN 9789811382963.
47. Siewert, M.; Neugebauer, F.; Epp, J.; Ploshikhin, V. Validation of Mechanical Layer Equivalent Method for Simulation of Residual Stresses in Additive Manufactured Components. *Comput. Math. Appl.* **2019**, *78*, 2407–2416. [CrossRef]
48. Simufact Engineering Gmbh MSC Software Company. *Simufact Additive Material Database 2020*; Simufact Engineering Gmbh MSC Software Company: Tokyo, Japan, 2020.
49. Li, Z.; Xu, R.; Zhang, Z.; Kucukkoc, I. The Influence of Scan Length on Fabricating Thin-Walled Components in Selective Laser Melting. *Int. J. Mach. Tools Manuf.* **2018**, *126*, 1–12. [CrossRef]
50. Shi, X.; Liu, X.; Ren, S.; Lu, P.; Xie, Z.; Wu, M. Selective Laser Melting Fabricated Tungsten with Thin-Walled Structure: Role of Linear Energy Density on Temperature Evolution and Manufacturing Quality. *Int. J. Mater. Form.* **2022**, *15*, 2. [CrossRef]
51. Cao, Q.; Bai, Y.; Zhang, J.; Shi, Z.; Fuh, J.Y.H.; Wang, H. Removability of 316L Stainless Steel Cone and Block Support Structures Fabricated by Selective Laser Melting (SLM). *Mater. Des.* **2020**, *191*, 108691. [CrossRef]